LETTERS
PUBLISHED ONLINE: 1 FEBRUARY 2009 | DOI: 10.1038/NPHYS1198
nature physics

Quantum interference and Klein tunnelling in graphene heterojunctions

Andrea F. Young and Philip Kim*

The observation of quantum conductance oscillations in mesoscopic systems has traditionally required the confinement of the carriers to a phase space of reduced dimensionality[1–4]. Although electron optics such as lensing[5] and focusing[6] have been demonstrated experimentally, building a collimated electron interferometer in two unconfined dimensions has remained a challenge owing to the difficulty of creating electrostatic barriers that are sharp on the order of the electron wavelength[7]. Here, we report the observation of conductance oscillations in extremely narrow graphene heterostructures where a resonant cavity is formed between two electrostatically created bipolar junctions. Analysis of the oscillations confirms that p–n junctions have a collimating effect on ballistically transmitted carriers[8]. The phase shift observed in the conductance fringes at low magnetic fields is a signature of the perfect transmission of carriers normally incident on the junctions[9] and thus constitutes a direct experimental observation of 'Klein tunnelling'[10–12].

Owing to the suppression of backscattering[13] and its amenability to flexible lithographic manipulation, graphene provides an ideal medium to realize the quantum engineering of electron wavefunctions. The gapless spectrum in graphene enables the creation of adjacent regions of positive and negative doping, offering an opportunity to study the peculiar carrier dynamics of the chiral graphene quasiparticles[8,10–12] and a flexible platform for the realization of a variety of unconventional electronic devices[14–17]. Previous experiments on graphene p–n junctions[18–25] were limited in scope by the diffusive nature of the transport beneath the local electrostatic gates; we overcome such limitations by fabricating extremely narrow (∼20 nm) local gates strongly capacitively coupled to the graphene channel (Fig. 1a,b). Electrostatics simulations based on finite-element analysis (see Supplementary Information) show that the carrier densities in the locally gated region (LGR) and the 'graphene leads'—n_2 and n_1, respectively—can be controlled independently by applying bias voltages to the top gate (V_{TG}) and the back gate (V_{BG}). The width of the LGR, L, is defined as the distance between the two zero-density points. As in previous studies[21], the conductance map as a function of V_{TG} and V_{BG} (Fig. 1c) can be partitioned into quadrants corresponding to the different signs of n_1 and n_2, with a lowered conductance observed when $n_1 n_2 < 0$. The mean free path in the bulk of the sample, $l_m \gtrsim 100$ nm, was extracted from the relation $\sigma = (2e^2/h)k_F l_m$ between the conductivity and Fermi momentum, k_F. As $L \lesssim 100$ nm within the experimentally accessible density regime, we expect a significant portion of the transport to be ballistic in the LGR.

In the bipolar regime, the diffusive resistance of the LGR is negligible in comparison with the highly resistive p–n junctions; as a result, the conductance does not increase with increasing magnitude of the charge density in the LGR (ref. 22). We note that the magnitude of this conductance step is only ∼60% as large as expected for a fully ballistic heterojunction even after taking into account the enhancement of the junction transparency due to nonlinear screening[26]; this suggests that there is still a large diffusive component to the transport through the heterojunction. Nevertheless, each trace exhibits an oscillating conductance as a function of V_{TG} when the carriers in the LGR and 'graphene leads' have opposite sign.

The regular structure of these oscillations is apparent when the numerical derivative of the measured conductance is plotted as a function of n_1 and n_2 (Fig. 2a). Although there is a weak dependence of the oscillation phase on n_1 reflecting the influence of the back gate on the heterojunction potential profile, the oscillations are primarily a function of n_2, confirming their origin in cavity resonances in the LGR. The oscillations, which arise from interference between electron waves in the LGR, are not periodic in any variables because of the strong dependence of the LGR width, L, and junction electric field, E, on the device electrostatics. Still, the conductance maxima are separated in density by roughly $\Delta n_2 \sim 1 \times 10^{12}$ cm^{-2}, in agreement with a naive estimate $\Delta n_2 \sim (4\sqrt{\pi n_2}/L)$ for the resonant densities in a cavity of width $L \sim 100$ nm. The application of an external magnetic field shifts the phase of the oscillations, with individual oscillation extrema moving towards higher density $|n_2|$ and the transmission resonances appearing to be adiabatically connected to the high-field Shubnikov–de Haas oscillations (Fig. 2d).

Graphene heterojunctions offer the opportunity to study an old problem in relativistic quantum mechanics: the tunnelling of relativistic electrons through a potential barrier[10,11]. In the context of the graphene p–n junction, this 'Klein tunnelling' manifests as the combination of the absence of backscattering with momentum conservation parallel to a straight p–n interface: normally incident particles, bound to conserve their transverse momentum, $k_y = 0$, and forbidden from scattering directly backwards, are predicted to tunnel through such symmetric potential barriers with unit probability. In contrast, particles obliquely incident on a barrier that is smooth on the atomic lattice scale encounter classically forbidden regions where the real part of the perpendicular momentum vanishes. These regions, which form about the centre of individual p–n junctions, transmit obliquely incident carriers only though quantum tunnelling, leading to an exponential collimation of ballistic carriers passing through graphene p–n junctions[8],

$$\left|T(k_y)\right|^2 = e^{-\pi\hbar v_F k_y^2/(eE)} \quad (1)$$

where v_F is the Fermi velocity of graphene.

Considerable experimental effort has been expended trying to verify equation (1) by matching bulk resistance measurements across a p–n junctions with their expected values[19,22,24]. Such an

Department of Physics, Columbia University, New York 10027, USA. *e-mail: pk2015@columbia.edu.

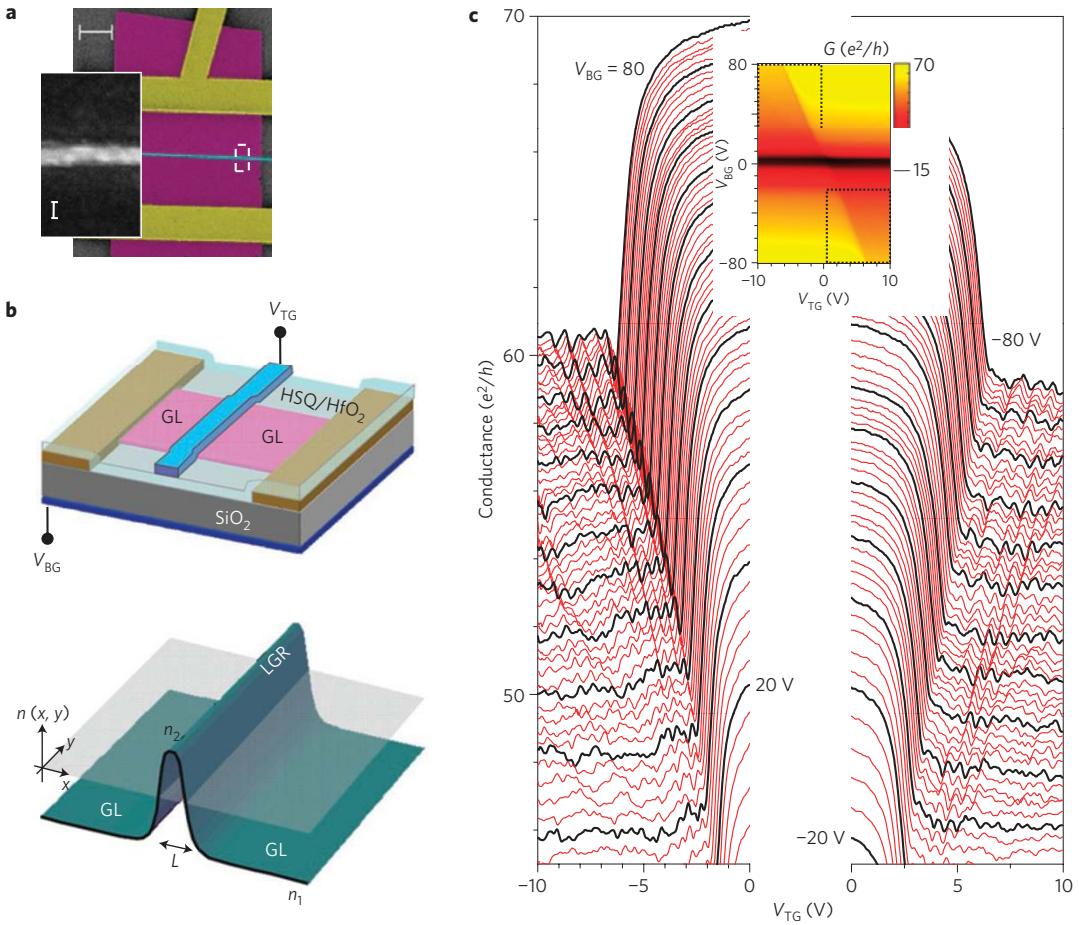

Figure 1 | Graphene heterojunction device schematic diagrams and conductance measurements. a, False-colour scanning electron microscope image of a typical graphene heterojunction device. Electrodes, graphene and top gates are represented by yellow, purple and cyan, respectively. The scale bar is 2 μm. Inset: High-magnification view of top gate. The scale bar is 20 nm. **b**, Schematic diagram of the device geometry. The electrostatic potential created by the applied gate voltages, V_{BG} and V_{TG}, can create a graphene heterojunction of width L bounded by two p–n junctions. GL: 'graphene leads'. **c**, The inset shows the conductance as a function of V_{TG} and V_{BG}. The main panels show cuts through this colour map in the regions indicated by the dotted lines in the inset, showing the conductance as a function of V_{TG} at fixed V_{BG}. Traces are separated by a step in V_{BG} of 1 V, starting from ±80 with traces taken at integer multiples of 5 V in black for emphasis.

approach can, at best, provide indirect evidence for the theoretically predicted features of chiral tunnelling—collimation and perfect transmission at normal incidence. In particular, there is no way to distinguish perfect from near-perfect transmission from a bulk resistance measurement, which is sensitive only to the total transparency of the p–n junction. The quantum interference experiments presented here enable a measurement not only of the magnitude but also the phase of the transmission and reflection coefficients. Interestingly, whereas the bulk of conduction in a fully ballistic graphene p–n junction is expected to be dominated by normally incident carriers, the absence of backscattering precludes the contribution of such trajectories to the Fabry–Perot resonances owing to perfect normal transmission at both interfaces. Rather, the oscillatory conductance receives its largest contributions from particles incident at angles where neither the transmission probability, $|T^2|$, nor the reflection probability, $|R|^2 = 1 - |T|^2$, are too large (see, for example, marker 1 in Fig. 2c). Only transmission near such angles contributes to the oscillatory conductance, ensuring the survival of the oscillations despite the incident angle averaging and enabling the determination of the width of the angle of acceptance of an individual collimating p–n junction.

In a ballistic heterojunction, the application of a magnetic field bends the carrier trajectories, resulting in an addition of an Aharonov–Bohm phase to the interference and a modification of the angle of incidence at each p–n junction. As was pointed out recently[9], such cyclotron bending leads to a direct experimental signature of reflectionless tunnelling, which manifests as a phase shift in the transmission resonances of a ballistic, phase coherent, graphene heterojunction at finite magnetic field. These resonances are described by the etalon-like ray-tracing diagrams shown in Fig. 2b. The Landauer formula for the oscillating part of the conductance is then

$$G_{\mathrm{osc}} = \frac{8e^2}{h} \sum_{k_y} |T_+|^2 |T_-|^2 |R_+||R_-| \cos(\theta_{\mathrm{WKB}} + \Delta\theta_{\mathrm{rf}}) \mathrm{e}^{-2L/l_{\mathrm{LGR}}} \qquad (2)$$

where $T_\pm$ and $R_\pm$ are the transmission and reflection amplitudes for the classically forbidden regions centred at $x = \pm L/2$, θ_{WKB} is the semiclassical phase difference accumulated between the junctions by interfering trajectories, $\Delta\theta_{\mathrm{rf}}$ is the Klein backreflection phase of the two interfaces and l_{LGR} is the mean free path in the locally gated region, a fitting parameter that controls the amplitude of the oscillations (see Supplementary Information).

At zero magnetic field, particles are incident at the same angle on both junctions, and the Landauer sum in equation (2) is dominated by modes that are neither normal nor highly oblique, as described above. As the magnetic field increases, cyclotron bending favours

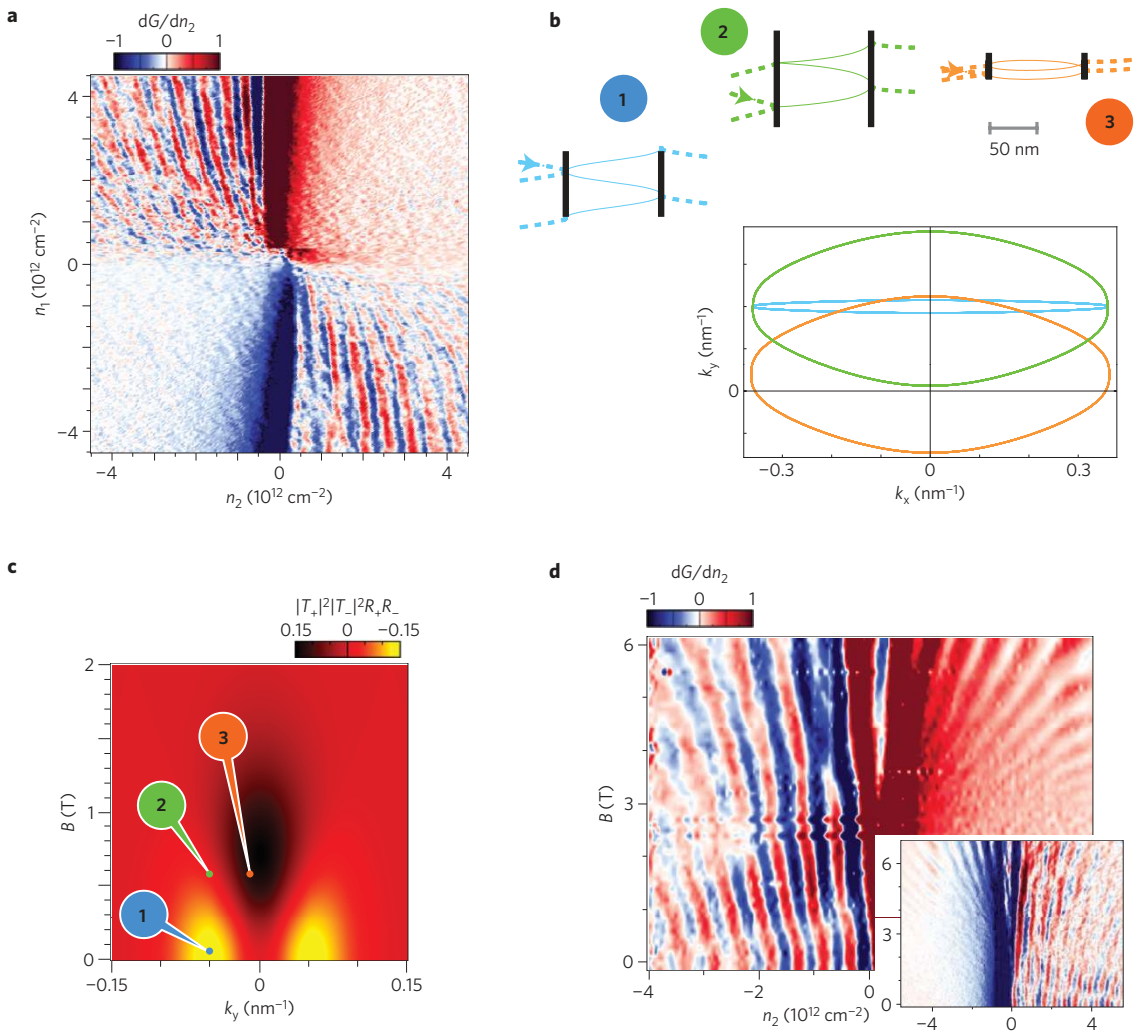

Figure 2 | Density and magnetic-field dependence of the oscillatory conductance; origin of the Klein tunnelling phase shift. a, dG/dn_2 as a function of n_1 and n_2. The scale bar is in arbitrary units. **b**, Schematic diagram of trajectories contributing to quantum oscillations in real and momentum space. The dominant modes at low magnetic field (marker 1) give way, with increasing B, to phase-shifted modes with negative reflection amplitude due to the inclusion of the non-trivial Berry phase (marker 3), near $k_y = 0$. The original finite k_y modes are not yet phase shifted at this field (marker 2), but owing to collimation, they no longer contribute to the oscillatory conductance. **c**, The prefactor in the Landauer sum, $|T_+|^2|T_-|^2R_+R_- = |T_+|^2|T_-|^2|R_+||R_-|e^{i\Delta\theta_{rf}}$, as a function of B and k_y, plotted for the experimental parameters at $V_{BG} = 50$ V for $n_2 = 3.5 \times 10^{12}$ cm^{-2}. The markers correspond to the trajectories shown in **b**. Regions of negative sign correspond to trajectories containing the Klein backscattering phase shift. **d**, Magnetic-field dependence of dG/dn_2 at $V_{BG} = 50$ V. Inset: Similar data taken at $V_{BG} = -50$ V. The magnetic phase is proportional to the sign of the carriers; as a result, the oscillation extrema precess in opposite directions for opposite signs of carriers in the LGR.

the contribution of modes with $k_y = 0$, which are incident on the junctions at angles with the same magnitude but opposite sign (see markers 2 and 3 in Fig. 2c). In the case of perfect transmission at zero incident angle, the reflection amplitude changes sign as the sign of the incident angle changes[9], causing a π shift in the phase of the reflection amplitudes. Equivalently, this effect can be cast in terms of the Berry phase: the closed momentum space trajectories of the modes dominating the sum at low field and high k_y do not enclose the origin, whereas those at intermediate magnetic fields and $k_y \sim 0$ do (Fig. 2b). Owing to the Dirac spectrum and its attendant chiral symmetry, there is a topological singularity at the degeneracy point of the band structure, $k_x = k_y = 0$, which adds a non-trivial Berry phase of π to trajectories surrounding the origin. As a consequence, the quantization condition leading to transmission resonances is different for such trajectories, leading to a phase shift in the observed conductance oscillations (that is, a π jump in $\Delta\theta_{rf}$) as the phase-shifted trajectories begin to dominate the Landauer sum in equation (2) (refs 27,28). For the electrostatics of the devices presented here, the magnetic field at which this phase shift is expected to occur is in the range $B^* = \sim$250–500 mT (see Supplementary Information), in agreement with experimental data (see Fig. 3a). As the magnetic field increases further, the ballistic theory predicts the disappearance of the Fabry–Perot conductance oscillations as the cyclotron radius, R_c, shrinks below the distance between p–n junctions, $R_c \lesssim L$, or $B \sim 2$ T for our devices. We attribute the apparent continuation of the oscillations to high magnetic field to the onset of disorder-mediated Shubnikov–de Haas type oscillations within the LGR.

To analyse the quantum interference contribution to the ballistic transport, we extract the oscillating part of the measured conductance by first antisymmetrizing the heterojunction resistance[19] with respect to the density at the centre of the LGR, $G_{odd}^{-1}(|n_2|) = G^{-1}(n_2) - G^{-1}(-n_2)$, and then subtracting a background conductance obtained by averaging over several oscillation periods in n_2, $G_{osc} = G_{odd} - \overline{G_{odd}}$. The resulting fringe pattern shows a marked phase shift at low magnetic field in accordance

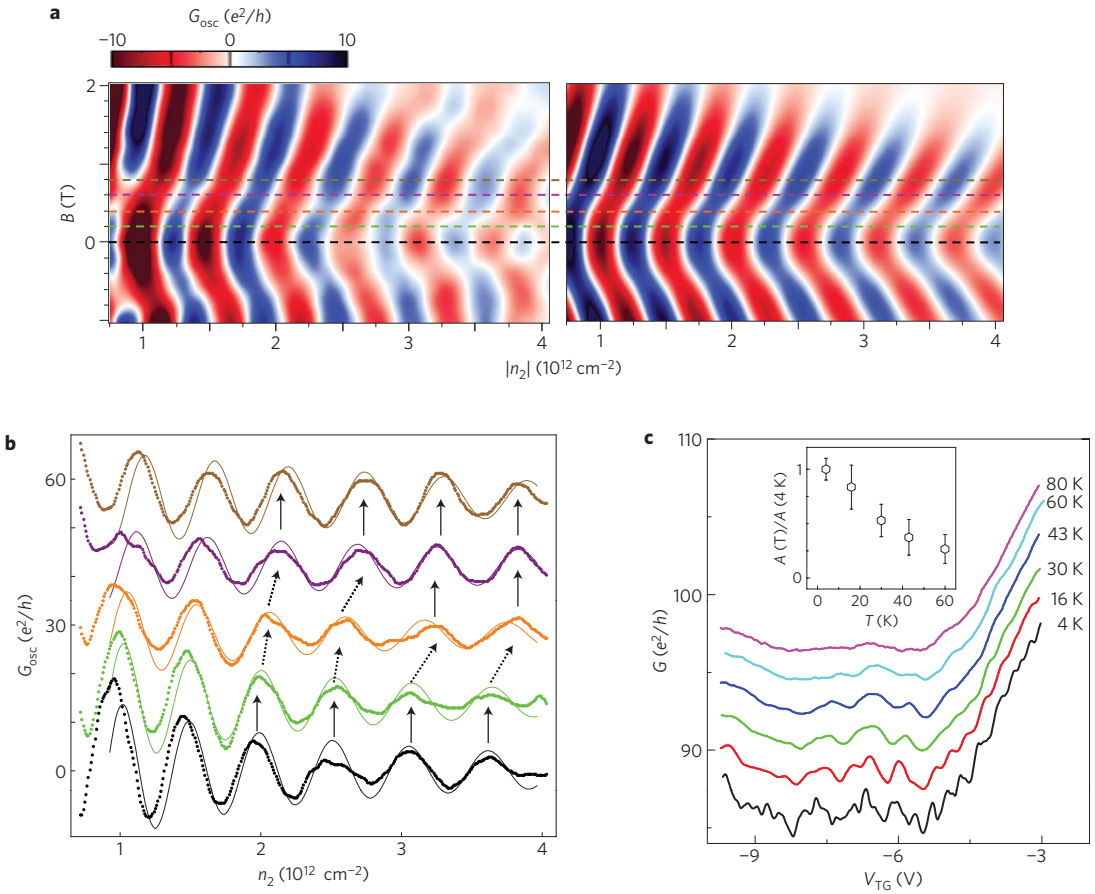

Figure 3 | Comparison of experimental data to the theoretical model, and temperature dependence. a, Magnetic-field and density dependence of the oscillating part of the conductance at $V_{BG} = 50$ V. G_{osc} as extracted from the experimental data (left panel) shows good agreement with a theoretical model accounting for nonlinear screening[26] (right panel) over a wide range of densities and magnetic fields. **b**, Cuts taken at $B = 0$, 200, 400, 600 and 800 mT, corresponding to the coloured dashed lines in **a**; the dots represent data, the smooth lines are the result of the simulations. The sudden phase shift that signals the presence of perfect transmission is indicated by dotted arrows. Curves are offset for clarity. **c**, Temperature dependence of the oscillation amplitude in a similar device to that presented in the rest of the text. The oscillations (different curves are offset for clarity) weaken with rising temperature, and are not observed above 80 K. At 4 K, the conductance modulations contain both the ballistic oscillations as well as aperiodic modulations due to mesoscopic conductance fluctuations, which quickly disappear with increasing temperature. Inset: Averaged amplitude of several oscillations, normalized by the amplitude at $T = 4$ K.

with the presence of the Klein backscattering phase, with two different regions—of unshifted and shifted oscillations—separated by the magnetic field B^* (see Fig. 3a). To carry out a quantitative comparison between the measured oscillating conductance and equation (2), we use numerical electrostatics simulations to determine the potential profile, which is then input into equation (2) to generate a fringe pattern for comparison with experimental data. We choose the free fitting parameter $l_{LGR} = 67$ nm for this comparison to best fit the oscillation amplitudes. Considering possible degradation of the graphene in and around the LGR during the fabrication of the local gates[29], this value is consistent with the estimate for the bulk mean free path. The resulting theoretical calculation exhibits excellent quantitative agreement with the experimental result at both zero and finite magnetic field (Fig. 3a,b), both in the magnitude and period of the oscillations. We emphasize that the value of L—which largely determines both the phase and amplitude of the oscillations—varies by almost a factor of three over the accessible density range, yet equation (2), faithfully describes the observed experimental conductance modulations in n_2 as well as in B. Such remarkable agreement confirms that the observed oscillatory conductance, which is controlled both by the applied gate voltage and the magnetic field, results from quantum interference phenomena in the graphene heterojunction. Moreover, the oscillations exhibit a phase shift at $B^* \sim 0.3$ T, which is the hallmark of perfect transmission at normal incidence, thus providing direct experimental evidence for the 'Klein tunnelling' of relativistic fermions through a potential barrier.

Finally, we turn our attention to the temperature dependence of the quantum coherence effects described in the text, which we observe at temperatures as high as 60 K (Fig. 3c). An elementary energy scale analysis suggests that the phase coherence phenomena should be visible at temperatures of order $(\hbar v_F/L) \sim 100$ K, when thermal fluctuations become comparable to the phase difference between interfering paths. In addition, the oscillation amplitude is sensitive to the carrier mean free path, and we attribute the steady waning of the oscillations with temperature to a combination of thermal fluctuations and further diminution of the mean free path by thermally activated scattering. The mean free path in clean graphene samples can be as large as ~1 μm (ref. 30), and a reduction of the width of the heterostructure L by an order of magnitude is well within the reach of modern fabrication techniques; consequently, technological improvements in the fabrication of graphene heterojunctions should lead to the observation and control of quantum coherent phenomena at much high temperatures, a crucial requirement for realistic, room-temperature quantum device applications.

Methods

Graphene sheets were prepared by mechanical exfoliation on Si wafers covered in 290 nm thermally grown SiO_2. Ti/Au contacts 5 nm/35 nm thick were deposited using standard electron beam lithography, and local gates subsequently applied using a thin (∼10 nm) layer of hydrogen silsesquioxane (HSQ) as an adhesion layer[21] for low-temperature atomic layer deposition of 20 nm of HfO_2, a high-k dielectric ($\epsilon \sim 12$) (see Fig. 1b). Palladium top gates not exceeding 20 nm in width were deposited to ensure that a sizeable fraction of conduction electrons remained ballistic through the LGR. Leakage current was measured to be $\lesssim$100 pA up to $V_{TG} = \pm 15$ V. All data except that in Fig. 3c were taken from the device shown in Fig. 1a, which had a measured mobility ∼5,000 $cm^2\,V^{-1}\,s^{-1}$. The data in Fig. 3d were taken from a similar device in a four-terminal Hall bar geometry; extra data from this device are shown in Supplementary Information. Several other similar devices were also measured, showing qualitatively similar behaviour. The conductance of the graphene devices was measured in a liquid-helium flow cryostat at 4.2–100 K using a standard lock-in technique with a current bias of 0.1–1 $\mu A_{r.m.s.}$ at 17.7 Hz. Unless otherwise specified, all measurements were done at 4.2 K. The ratio $C_{TG}/C_{BG} \approx 12.8$ was determined from the slope of the Dirac ridge with respect to the applied voltages, and similar values were obtained from the analysis of the period of the Shubnikov–de Haas oscillations in magnetic field, which also served to confirm the single-layer character of the devices. Finite-element electrostatics simulations were carried out for the measured device geometries described above with the thickness and dielectric constant of the HSQ adjusted such that the simulations matched the observed values of C_{TG}/C_{BG}. The shape of the potential and the strength of the electric field E used in fitting the experimental data were constrained to lie within the confidence interval of the simulations, which in turn were largely determined by uncertainty in the device geometry.

Received 7 August 2008; accepted 23 December 2008; published online 1 February 2009

References

1. van Wees, B. J. *et al.* Observation of zero-dimensional states in a one-dimensional electron interferometer. *Phys. Rev. Lett.* **62**, 2523–2526 (1989).
2. Ji, Y. *et al.* An electronic Mach-Zehnder interferometer. *Nature* **422**, 415–418 (2003).
3. Liang, W. *et al.* Fabry–Perot interference in a nanotube electron waveguide. *Nature* **411**, 665–669 (2001).
4. Miao, F. *et al.* Phase-coherent transport in graphene quantum billiards. *Science* **317**, 1530–1533 (2007).
5. Spector, J., Stormer, H. L., Baldwin, K. W., Pfeiffer, L. N. & West, K. W. Electron focusing in two-dimensional systems by means of an electrostatic lens. *Appl. Phys. Lett.* **56**, 1290–1292 (1990).
6. van Houten, H. & Beenakker, C. W. J. in *Analogies in Optics and Micro Electronics* (eds van Haeringen, W. & Lenstra, D.) (Kluwer, 1990).
7. Washburn, S., Fowler, A. B., Schmid, H. & Kern, D. Possible observation of transmission resonances in GaAs–Al_xGa_{1-x} As transistors. *Phys. Rev. B* **38**, 1554–1557 (1988).
8. Cheianov, V. V. & Fal'ko, V. I. Selective transmission of Dirac electrons and ballistic magnetoresistance of n–p junctions in graphene. *Phys. Rev. B* **74**, 041403(R) (2006).
9. Shytov, A. V., Rudner, M. S. & Levitov, L. S. Klein backscattering and Fabry–Perot interference in graphene heterojunctions. *Phys. Rev. Lett.* **101**, 156804 (2008).
10. Katsnelson, M. I., Novoselov, K. S. & Geim, A. K. Chiral tunnelling and the Klein paradox in graphene. *Nature Phys.* **2**, 620–625 (2006).
11. Klein, O. Die Reflexion von Elektronen an einem Potentialsprung nach der relativistischen Dynamik von Dirac. *Z. Phys.* **53**, 157–165 (1929).
12. Sauter, F. Über das Verhalten eines Elektrons im homogenen elektrischen Feld nach der relativistischen Theorie Diracs. **69** 742–764 (1931).
13. Ando, T. & Nakanishi, T. Impurity scattering in carbon nanotubes: Absence of backscattering. *J. Phys. Soc. Jpn.* **67**, 1704–1713 (1998).
14. Cheianov, V. V., Fal'ko, V. I. & Altshuler, B. L. The focusing of electron flow and a Veselago lens in graphene p–n junctions. *Science* **315**, 1252–1255 (2007).
15. Park, C.-H. *et al.* Anisotropic behaviours of massless Dirac fermions in graphene under periodic potentials. *Nature Phys.* **4**, 213–217 (2008).
16. Park, C.-H. *et al.* Electron beam supercollimation in graphene superlattices. *Nano Lett.* **8**, 2920–2924 (2008).
17. Garcia-Pomar, J. L., Cortijo, A. & Nieto-Vesperinas, M. Fully valley-polarized electron beams in graphene. *Phys. Rev. Lett.* **100**, 236801 (2008).
18. Lemme, M. C., Echtermeyer, T. J., Baus, M. & Kurz, H. A graphene field effect device. *IEEE Electron Device Lett.* **28**, 282–284 (2007).
19. Huard, B. *et al.* Transport measurements across a tunable potential barrier in graphene. *Phys. Rev. Lett.* **98**, 236803 (2007).
20. Williams, J. R., DiCarlo, L. & Marcus, C. M. Quantum Hall effect in a gate-controlled p–n junction of graphene. *Science* **317**, 638–641 (2007).
21. Özyilmaz, B. *et al.* Electronic transport and quantum Hall effect in bipolar graphene p–n–p junctions. *Phys. Rev. Lett.* **99**, 166804 (2007).
22. Gorbachev, R. V., Mayorov, A. S., Savchenko, A. K., Horsell, D. W. & Guinea, F. Conductance of p–n–p graphene structures with air-bridge top gates. *Nano Lett.* **8**, 1995–1999 (2008).
23. Liu, G., Velasco, J., Bao, W. & Lau, C. N. Fabrication of graphene p–n–p junctions with contactless top gates. *Appl. Phys. Lett.* **92**, 203103 (2008).
24. Stander, N., Huard, B. & Goldhaber-Gordon, D. Evidence of Klein tunneling in graphene p–n junctions. Preprint at <http://arxiv.org/abs/0806.2319> (2008).
25. Meric, I. *et al.* Current saturation in zero-bandgap, top-gated graphene field-effect transistors. *Nature Nanotech.* **3**, 654–659 (2008).
26. Zhang, L. M. & Fogler, M. M. Nonlinear screening and ballistic transport in a graphene p–n junction. *Phys. Rev. Lett.* **100**, 116804 (2008).
27. Novoselov, K. S. *et al.* Two-dimensional gas of massless Dirac fermions in graphene. *Nature* **438**, 197–200 (2005).
28. Zhang, Y., Tan, Y. W., Stormer, H. L. & Kim, P. Experimental observation of the quantum Hall effect and Berry's phase in graphene. *Nature* **438**, 201–204 (2005).
29. Ryu, S. *et al.* Reversible basal plane hydrogenation of graphene. *Nano Lett.* **8**, 4597–4602 (2008).
30. Bolotin, K. I. *et al.* Ultrahigh electron mobility in suspended graphene. *Solid State Commun.* **146**, 351–355 (2008).

Acknowledgements

The authors would like to thank I. L. Aleiner, K. I. Bolotin, M. Y. Han, E. A. Henriksen, L. S. Levitov and H. L. Stormer for discussions, and I. Meric and M. Y. Han for help with sample preparation. This work is supported by the ONR (No. N000150610138), FENA, NRI, NSEC (No. CHE-0117752) and NYSTAR. Sample preparation was supported by the DOE (DE-FG02-05ER46215).

Additional information

Supplementary Information accompanies this paper on www.nature.com/naturephysics. Reprints and permissions information is available online at http://npg.nature.com/reprintsandpermissions. Correspondence and requests for materials should be addressed to P.K.